Angewandte Chemie

Eine Zeitschrift der Gesellschaft Deutscher Chemiker

www.angewandte.de

Akzeptierter Artikel

Titel: Creating High-entropy Single Atoms on Transition Disulfides through Substrate-induced Redox Dynamics for Efficient Electrocatalytic Hydrogen Evolution

Autoren: zhaoyan luo, Yirun Guo, Changjie He, Yi Guan, Lei Zhang, Yongliang Li, Qianling Zhang, Chuanxin He, Xueliang Sun, and Xiangzhong Ren

Zitierweise: *Angew. Chem. Int. Ed.* **2024**, e202405017

Link zur VoR: https://doi.org/10.1002/anie.202405017

WILEY VCH

10.1002/ange.202405017

WILEY VCH

RESEARCH ARTICLE

Creating High-entropy Single Atoms on Transition Disulfides through Substrate-induced Redox Dynamics for Efficient Electrocatalytic Hydrogen Evolution

Zhaoyan Luo[a], Yirun Guo[a], Changjie He[a], Yi Guan[b], Lei Zhang[a], Yongliang Li[a], Qiangling Zhang[a], Chuanxin He[a], Xueliang Sun* [b,c], Xiangzhong Ren* [a]

[a] Z. Luo, Y. Guo, C. He, L. Zhang, Y. Li, Q. Zhang, C. He, X. Ren
College of Chemistry and Environmental Engineering, Shenzhen University, Shenzhen 518071, China
E-mail: renxz@szu.edu.cn

[b] Y. Guan, X. Sun
Department of Mechanical and Materials Engineering, University of
Western Ontario, London, ON, N6 A 5B9, Canada
E-mail: xsun9@uwo.ca

[c] X. Sun
Eastern Institute for Advanced Study, Eastern Institute of Technology, Ningbo, Zhejiang 3150200, China

Supporting information for this article is given via a link at the end of the document.

Abstract: The controllable anchoring of multiple metal single-atoms (SAs) into a single support exhibits scientific and technological opportunities, while marrying the concentration-complex multimetallic SAs and high-entropy SAs (HESAs) into one SAC system remains a substantial challenge. Here, we present a substrate-mediated SAs formation strategy to successfully fabricate a library of multimetallic SAs and HESAs on MoS_2 and $MoSe_2$ supports, which can precisely control the doping location of SAs. Specially, the contents of SAs can continuously increase until the accessible Mo atoms on TMDs carriers are completely replaced by SAs, thus allowing the of much higher metal contents. In-depth mechanistic study shows that the well-controlled synthesis of multimetallic SAs and HESAs is realized by controlling the reversible redox reaction occurred on the TMDs/TM ion interface. As a proof-of-concept application, a variety of SAs-TMDs were applied to hydrogen evolution reaction. The optimized HESAs-TMDs (Pt,Ru,Rh,Pd,Re-$MoSe_2$) delivers a much higher activity and durability than state of-the-art Pt. Thus, our work will broaden the family of single-atom catalysts and provide a new guideline for the rational design of high-performance single-atom catalysts.

Introduction

Improving the atomic economics of chemical transformation and ensuring maximum use of scarce catalytic materials are core objectives of sustainable chemistry[1]. Heterogeneous single-atom catalysts (SACs), integrating highly dispersed metal sites with customizable support materials, demonstrate the potential to achieve both goals in several energy-related conversions[2]. Moreover, SACs provide a basic platform for exploring structure-activity relationships and studying catalytic mechanisms at the atomic scale, owing to the highly uniform active centres and tunable coordination environment[3]. These exciting features has inspired the development of integrated synthesis strategies for single-atom catalysts. Despite great progress in this area, several great challenges remain. First, it is a great challenge to achieve the stabilization of transition metals (TM) as isolated centres with high areal density on carriers, because metal single atoms tend to aggregate into metals clusters/particles, especially at high metal loading, owing to the Gibbs–Thomson effect[4]. Second, to create the SACs with the types of precisely customized catalytic interface that enable targeted properties and applications, understanding the formation process of SAs on support is crucial for the rational design of novel SACs model catalysts. Unfortunately, due to the ambiguous interaction between metal single atoms and supports, there is no unified guiding principle that govern the formation of SAs on supports; in particular, different metallic centres possess different chemical and electronic properties[5], thus the synthesis guidelines for one SA cannot simply be extrapolated to another SA. Third, until now, there has been a knowledge gap in how to marry multiple isolated metals atoms into a single support and open up polymetallic phase spaces with complex concentrations for SAs, which is much more complex than traditional SAs that containing only one or two metallic SAs[6]; thus, developing a general synthesis method to prepare polymetallic SAs and high-entropy SAs is expected to open a new window for both improving the catalytic performance and advancing the mechanistic understanding of heterogeneous catalysis, which also remains a challenge and has been rarely reported.

Two-dimensional transition metal disulfides (TMDs) as a carrier for immobilized SACs promises to resolve these challenges. Compared to carbon-related carriers [7], which is chemically inert

10.1002/ange.202405017

RESEARCH ARTICLE

and thus challenging to functionalize without interfering with the body structure, TMDs are bound by chalcogen atoms (e.g., S, Se)—elements that own Lewis base properties with lone pair electrons and appropriate electronegativity — may potentially interact with, and hence stabilize SAs. Furthermore, the SAs interact strongly with surface anions and anion vacancies in TMDs surface, resulting in high metal dispersion in the absence of agglomeration. In particular, TMDs may provide a good platform for understanding the formation processes of SAs, owing to the well-defined electronic band structure and strong metal–support interaction. Additionally, these TMDs materials are particularly studied as efficient catalysts for photocatalysis, electrocatalysis [8]. Therefore, it is necessary to study a general method for preparing high-loading of multimetallic SAs supported on TMDs and elucidate formation process.

Herein, we present a substrate-mediated SAs formation strategy to fabricate a library of TM-SAs on TMDs (MoS_2, $MoSe_2$) with an ultra-high TM-atom densities of up to 40 wt % (in the case of Pt and Pd). Our strategy relies on the reversible redox reaction occurred on the TMDs/TM ion interface. According to the principles of defect chemistry, structural vacancies can be created on the TMD surface during the redox process. These vacancy sites offered numerous coordination points for anchoring TM-SA, thus resulting in a high density of SAs with strong TM-support interaction. This is applicable to a library of reducible TMs including noble and non-noble TMs (Cu, Ag, Pt, Ru, Ir, Rh, Pd, Au etc). Most notably, we utilize the library to open up complex multimetallic phase spaces via implanting the multiple isolated metal atoms into a TMD support to fabricate the multimetallic SAs and high-entropy SAs (HESAs), and found that there is no fundamental limit on using single-atom anchor sites as structural units to assemble the concentration-complex the multimetallic SAs and HESAs. To prove utility, the HESAs is investigated as hydrogen evolution reaction catalyst with much lower overpotential and durability than commercial Pt/C catalyst in alkaline media.

Results and Discussion

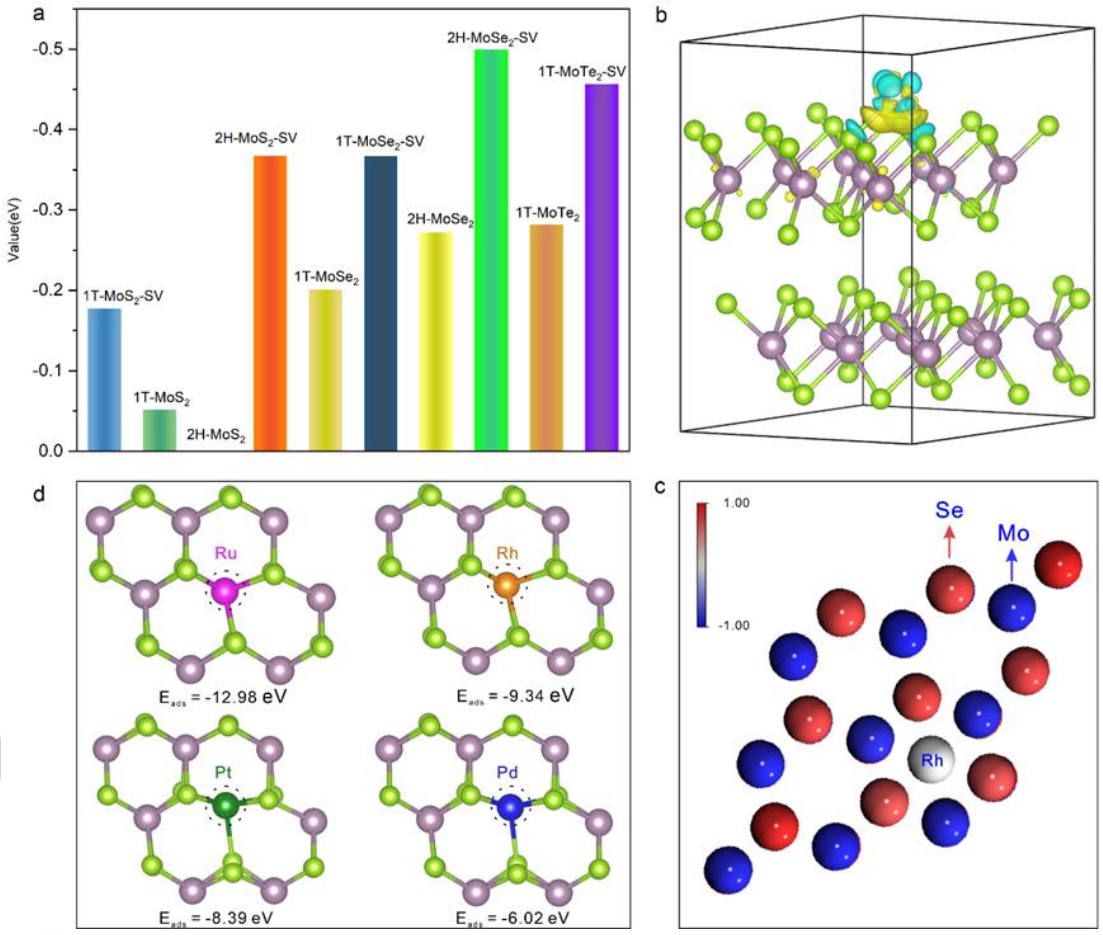

Figure 1. **a** A band alignment diagram for bulk 2H-MoS_2, 2H-$MoSe_2$, 1T-MoS_2, 1T-$MoSe_2$, 1T-$MoTe_2$ and its corresponding materials containing chalcogen vacancies, respectively. Here, the 2H-MoS_2 material is used as the benchmark. **b** Single-atom adsorption of Rh on 2H-$MoSe_2$ bulk material with charge transfer analyses. **c** Bader charge analysis of Rh single atom adsorbed on the 2H-MoSe2 bulk material. **d** Top views of the DFT calculated geometries for TM (Ru, Rh, Pt, Pd) on the Mo vacancy sites in $MoSe_2$ and corresponding the adsorption energy (E_{ads}).

10.1002/ange.202405017

The design of high-loading monometallic SAs, multimetallic SAs and HESAs is based on the redox characteristics of TMDs. As we all know, the chemically synthesized TMDs usually contain a certain concentration of defects such as chalcogen vacancies. These chalcogen vacancies are electron donors that can induce localized gap state in TMDs, thereby endowing TMDs with redox power. We have revealed in our recent work that some metal cations such as Pd^{2+}, Au^{3+} and Pt^{2+} can be reduced by MoS_2 nanosheets[9]. More interestingly, some reduced metal single atoms (Pd, Ru) can also be spontaneously doped into the Mo vacancy sites during the redox reaction process, simultaneously causing the sulfur vacancies generation and the phase transition from 2H to 1T phase. The abundant SVs and the phase transition can further drive the interfacial redox reaction. Such processes may represent a scalable approach to manufacturing high-loading single-atom catalysts that are directly anchored to the TMDs surfaces, including monometallic SAs, 2-, 3- metal and high entropy SAs.

We began by recognizing the redox characteristics of TMDs using a combination of experimental and theoretical techniques. The redox power of TMDs were first confirmed by the experimental phenomenon that TMD nanosheets such as MoS_2 and $MoSe_2$ can reduce Au^{3+} at room temperature without additional reducing agents, shown in Figure S1-3 and Supplementary Note 1. Moreover, we found that the final samples of Au-$MoSe_2$ shows only the Mo of the IV valence state compared to the mixed valence states of Mo^{3+} and Mo^{4+} in the pristine $MoSe_2$ and MoS_2, indicating that all Mo^{3+} is completely oxidized to Mo^{4+}. Meanwhile, the Au^{3+} precursors was converted to the Au(0) metallic states in the resulting Au-$MoSe_2$ and Au-MoS_2. From this, it can be determined the reactions occurred through Equation 1 and 2 in the following, where Mo^{3+} acts as a reducing agent to reduce a class of transition metal ions (such as Pt^{4+}, Rh^{3+}, Pd^{2+}, et al).

$$Mo(IV) + e^- \rightarrow Mo(III) \quad (\varphi^{\theta}Mo(IV) / Mo(III) = -0.04\ V) \qquad \text{Equation 1}$$

$$3Mo(III) + HAuCl_4 \rightarrow Au(0) + 3\,Mo(IV) + 4HCl \quad (\Delta rG^{\theta} = -280.815\ kJ) \qquad \text{Equation 2}$$

Then, the theoretical calculations were further carried out to investigate why TMDs can reduce the metal cations. First, we compared the redox power of a library of TMDs. As shown in Figure 1a and Table S1, the Fermi levels values of MoS_2, $MoSe_2$ and $MoTe_2$ bulk materials aligned with the core levels are 64.71 eV, 64.43 eV and 64.42 eV, which indicates that the redox power of MoS_2 is lower than that of other TMD materials. Second, we investigated how chalcogen vacancies on the TMDs surface affect the energetics of the metal cations reduction process on this library of TMDs. We found that the introduction of chalcogen vacancies would elevate the valence band maximum of the TMDs; meanwhile, the Fermi levels of TMDs decreases slightly when chalcogen defects are introduced. These changes will facilitate the reduction of metal cations, thus chalcogen defects play an important role in regulating the redox power of TMDs. Furthermore, crystal phase is also a key factor determining the redox characteristics of TMD materials. We calculated the Fermi level for 1T phase- and 2H phase- TMDs, and it is found that the Fermi level also decreased when the crystal phases of TMDs are converted from semiconducting 2H to metallic 1T-phase. As we known, the charge transfer between the TMDs and metal is very favorable evidence to support that the metal can be reduced by TMDs. We then conducted DFT calculations to obtain deeper atomic-level insights into the electronic interactions between the reduction metal and the TMDs. For Rh/2H-$MoSe_2$ as an example, the charge density difference diagrams (Figure 1b) clearly show the charge transfer occurring in the $MoSe_2$−Rh interface. Moreover, the Bader analysis (Figure 1c and Figure S4) also reveals that the charge transfer from an adsorbed TMs atom to $MoSe_2$. Therefore, the computational results also confirm that the metal reduction on TMDs surface is thermodynamically favourable. According to the charge conservation principle in defect chemistry, Mo(III) oxidation can create Mo vacancies on TMD nanosheets. Due to the high surface energy, reduced metal single atoms may migrate to these Mo vacancy sites. To confirm my hypothesis, we further calculated the energy for the formation of Mo vacancy (V_{Mo}) in pristine $MoSe_2$ surface and the $MoSe_2$ surface adsorbed by TMs atom (Figure S5). The energy for V_{Mo} formation decreased by ~0.1-0.9 eV due to the TMs atoms adsorption, which indicates that using the spontaneous interfacial redox reaction strategy to create the Mo vacancy on the $MoSe_2$ is also theoretically possible. Furthermore, we further calculated the energies of metal dopants at TMD surface and Mo vacancy sites. As shown in Figure 1d and Figure S5-7), these reduced metal atoms (Ir, Rh, Pd, Ru, Pt) exhibit strong tendencies to replace Mo vacancy sites compared to adsorbed on the Mo atop sites, thus supporting our expectation of the thermodynamically driven formation of the single-atom catalysts that are directly anchored to the TMDs backbone.

Here, we synthesized a large library of ultrahigh-loading monometallic SAs, multimetallic SAs and high entropy SAs (HESAs) via a substrate-mediated SAs formation strategy. The approach relies on the inter-valence charge transfer between Mo(III) and Mo(IV) ions on substrate. The introduction of metal single atom occurs in a two-step mechanism (see Supplementary Note 2). First, the standard redox potential (SRP) between Mo^{3+}

10.1002/ange.202405017

and Mo^{4+} is -0.04 V, theoretically reducing any redox couples with a higher SRP (Ru/Ru^{3+}, Rh/Rh^{3+}, etc) (Supplementary Note 3). The spontaneous interfacial TMDs/TM ion redox reaction will lead to the reduction of transition metal (TM) ion and oxidation of Mo^{3+}, thus creating Mo vacancies on TMD surface due to the charge conservation principle; following reduction, TM(0) single atoms are thermodynamically favorable for anchoring to the energetic Mo vacancies and are spontaneously embedded into the lattice of TMDs; At the same time, Mo^{4+} is reduced back to Mo^{3+}, thereby releasing its reducing power. Thus, it is theoretically possible to continuously increase the doping content of TM single atoms until the accessible Mo atoms are completely replaced by TM metal atoms, thus allowing the of much higher metal contents.

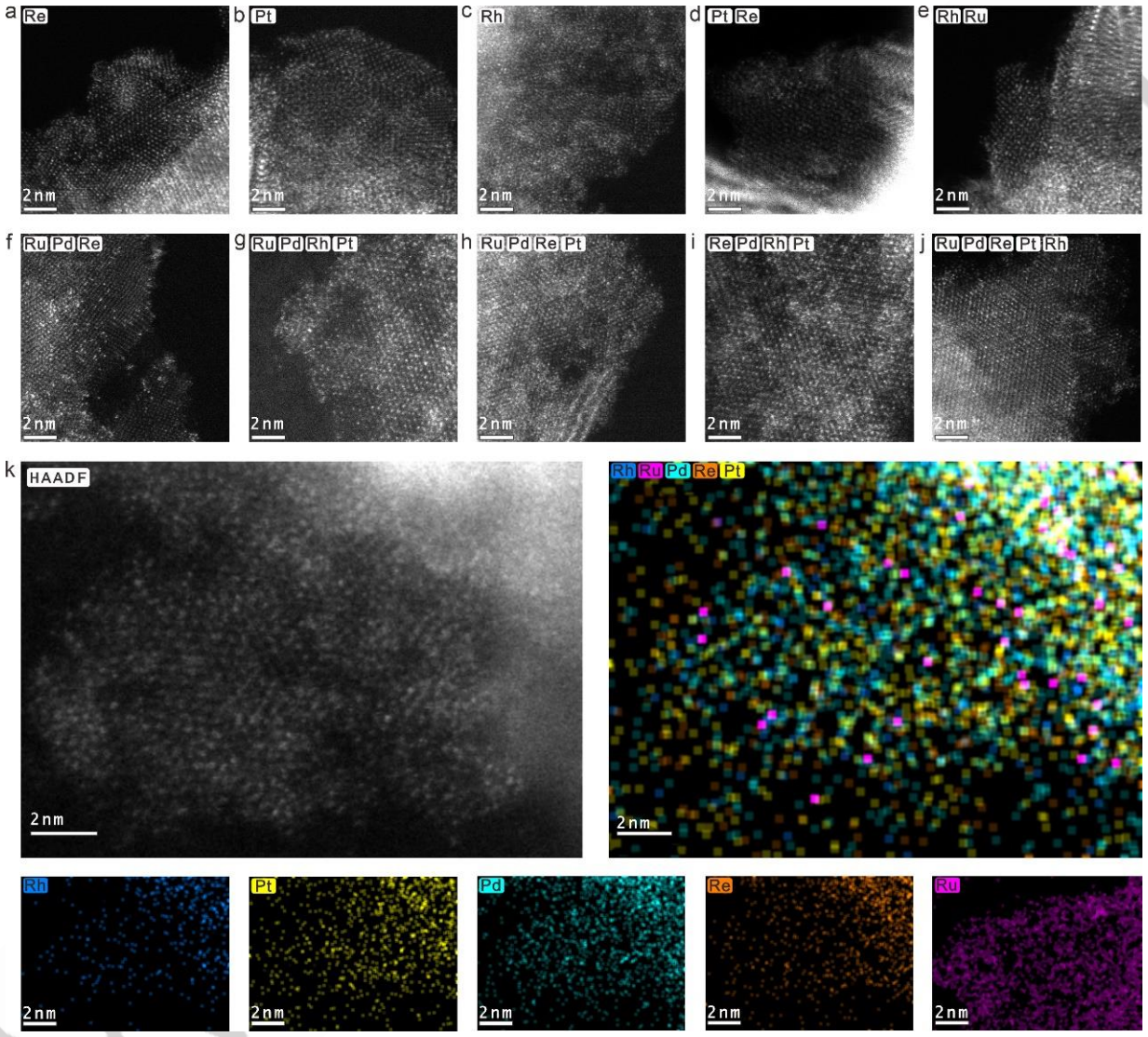

Figure 2. **a-j** Aberration-corrected HAADF-STEM images of high-loading monometallic SAs, multimetallic SAs and HESAs supported on TMDs. Scale bars, 2 nm. k EDS mapping of Ru, Pd, Re, Rh and Pt in Pt, Ru, Rh, Pd,Re-$MoSe_2$. Scale bars, 2 nm.

Inductively coupled plasma atomic emission spectrometry (ICP-AES) analysis has shown that the spontaneous interfacial redox technique achieves metal contents higher than 15 wt%, in several cases exceeding 49 wt% (Table S2). Here, we also achieved the formation of multimetallic SAs and HESAs, such as 2-, 3- ,4- and 5-metal SAs, through using similar procedures[10]. The structural data of the high-loading monometallic SAs, multimetallic SAs and HESAs were evaluated by the scanning electron microscopy (SEM), transmission electron microscopy (TEM), X-ray diffraction (XRD) and aberration-corrected high-angle annular dark-field scanning transmission electron microscopy (HAADF-STEM). The SEM and TEM patterns (Figure S8-13) reveal that all the as-prepared samples are composed of two-dimensional nanosheets, and the morphology of TMD materials are well retained after heteroatom doping. Additionally, no nanoparticles or large clusters appeared in the TEM images, which ruled out the

10.1002/ange.202405017

formation of metal sulfides. XRD pattern (Figure S14-15) also shows that the corresponding TMs has no crystallization characteristics. The HAADF-STEM images (Figure 2a-c and Figure S16-18) exhibit an ordered TMDs crystal structure after dopant fixation, which is evidence for the dispersion of dopant atoms. From the HAADF-STEM patterns, we can see that these HESAs-TMD systems display high metal atom densities and heavy elements such as rhenium, rhodium and platinum, which are distinguishable on TMD nanosheets, also evidence atomic dispersion. HAADF-STEM images of 2-, 3-, 4-polymetallic and high-entropy materials (Figure 2d-j) also confirm the atomic dispersion of component metals in polymetallic and high-entropy systems. The energy-dispersive X-ray spectroscopy (EDS) of TMDs-based SAs systems reveals that the spatial uniformity of individual elements in multimetallic and high entropy systems (Figure 2k and Figure S18).

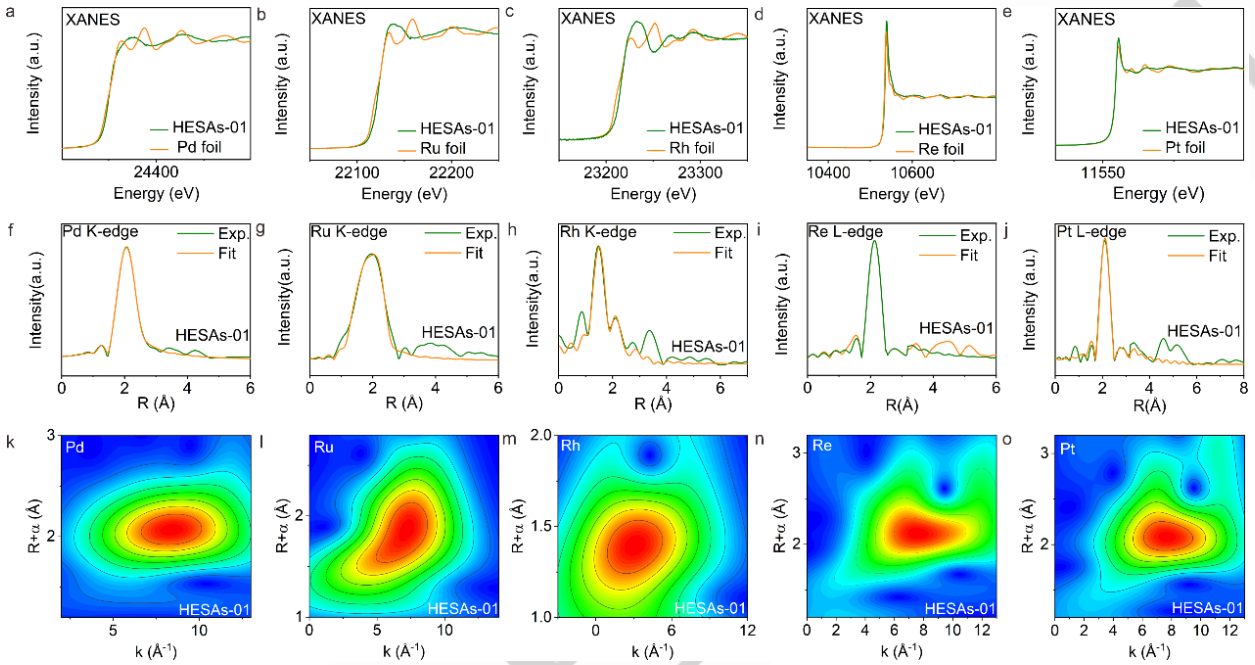

Figure 3. **a-e** XANES spectra for high-loading monometallic SAs, multimetallic SAs and HESAs supported on TMDs. **f-j** FT-EXAFS spectra for high-loading monometallic SAs, multimetallic SAs and HESAs supported on TMDs. **k-o** corresponding WT-EXAFS plots. (Here, HESAs-01 and HESAs-02 refer to Pt,Ru,Rh,Pd,Re-$MoSe_2$, Pt,Ru,Rh,Pd,Re-MoS_2, respectively.)

X-ray photoelectron spectroscopy (XPS), X-ray absorption near-edge structure (XANES), extended X-ray absorption fine structure (EXAFS) spectrometry and time‐of‐flight secondary ion mass spectrometry (ToF−SIMS) were further carried out to elucidate the local environment of metal atoms, thus confirming the presence of monometallic SAs, multimetallic SAs and high entropy SAs in various TMD nanosheets. The high-resolution XPS spectra (Figure S19) of TM-SAs show the formation of metal-sulfur bonds in all samples and support the substitutional dopants within the TMDs lattice. The XPS of Pt,Ru,Rh,Pd,Re-$MoSe_2$ shows the presence of these Pt, Ru, Rh, Pd and Re elements, the atomic ratio of Pt, Ru, Rh, Pd and Re was close to 1:1:1:1:0.6, further confirming that the HESAs was successfully prepared. The bulk compositions, especially for the metal elements were also evaluated by inductively coupled plasma optical emission spectrometer (ICP-OES), as illustrated in Table S2. The ICP of Pt,Ru,Rh,Pd,Re-$MoSe_2$ also shows the presence of these Pt, Ru, Rh, Pd and Re elements, the atomic ratio of Pt, Ru, Rh, Pd and Re was close to 1.1:1.2:1:0.9:0.7, further confirming that the HESAs was successfully prepared. Further, the XPS patterns also reveal that the oxidation. The oxidation states of TM-SAs centres were further validated by the XANES (Figure 3a-e and Figure S20). The XANES spectra also reveal that the absorption-edge of TM-SAs is obviously higher than that of corresponding metal foil, indicating that the TM species was oxidized after doping TMDs. Figure 3f-j and Figure S21-27 show k^3-weighted R-space Fourier transform spectra of EXAFS for the SAs. For each TM-SAs, the spectrum was distinct from that of the relevant TM foil. All SAs contain a single peak in the first shell in R space at around 1.80 Å. This distance is shorter than the typical TM-TM bond distance of TM foil, indicating that the TM species are atomically dispersed on the TMD nanosheets. The Fourier transform EXAFS fitting identifies that all TM atoms coordinated with the chalcogen atoms (S and Se). The intensity maximum possesses different coordinates (k, R), whose location is mainly connected with the

10.1002/ange.202405017

RESEARCH ARTICLE

path length R and atomic number Z. We further carried out the wavelet-transform (WT) EXAFS to provide additional k-space information, shown in Figure 3k-o. For every TM-SAs, only a predominant intensity maximum at lower k space was detected in these TM-SAs, and the absence of corresponding M-M metallic path further certified that no metal nano crystallites are present in these samples. For each TM-SAs, only one dominant intensity maximum was detected in the low k space, and there was no corresponding M-M scattering path, further supporting the absence of metal nanocrystals in these samples. Moreover, the best fitting of k^2-weighted TM (TM: Pd, Ru, Pt, Rh, Re) K-edge FT spectrum of all SAs–TMDs systems exhibits similar profile and fitting parameters to that of Mo in TMDs (Table S4-11), indicates that TM substitute Mo atoms in TMDs. However, because the scattering paths of the second shell TM-Mo are similar, it is challenging to determine the exact location of TM in multimetallic SACs and high entropy SAs systems using only EXAFS spectroscopy. Thus, we carried out ToF - SIMS to further determine the detailed structural of final catalyst. Here, we used the ToF-SIMS to examine the structure of Pt,Ru,Pd,Re-MoS_2 sample. As shown in Figure S28, Pd,Pt,Ru,Re-MoS_{2-x} clearly demonstrates a range of fragmented structures of Mo, S, MoS, and several metal fragment such as: Re+Mo, Pt+Ru, Mo+Ru+Pd, Re+Mo+Pd, Re+Ru+Pd+S, et al being detected. Given that the fragments such as these metal fragments are also possibly derived from breakage of Pd,Pt,Ru,Re-MoS_2 in the substrate, unambiguously demonstrating that the multimetallic SAs and high entropy SAs were successfully synthesized.

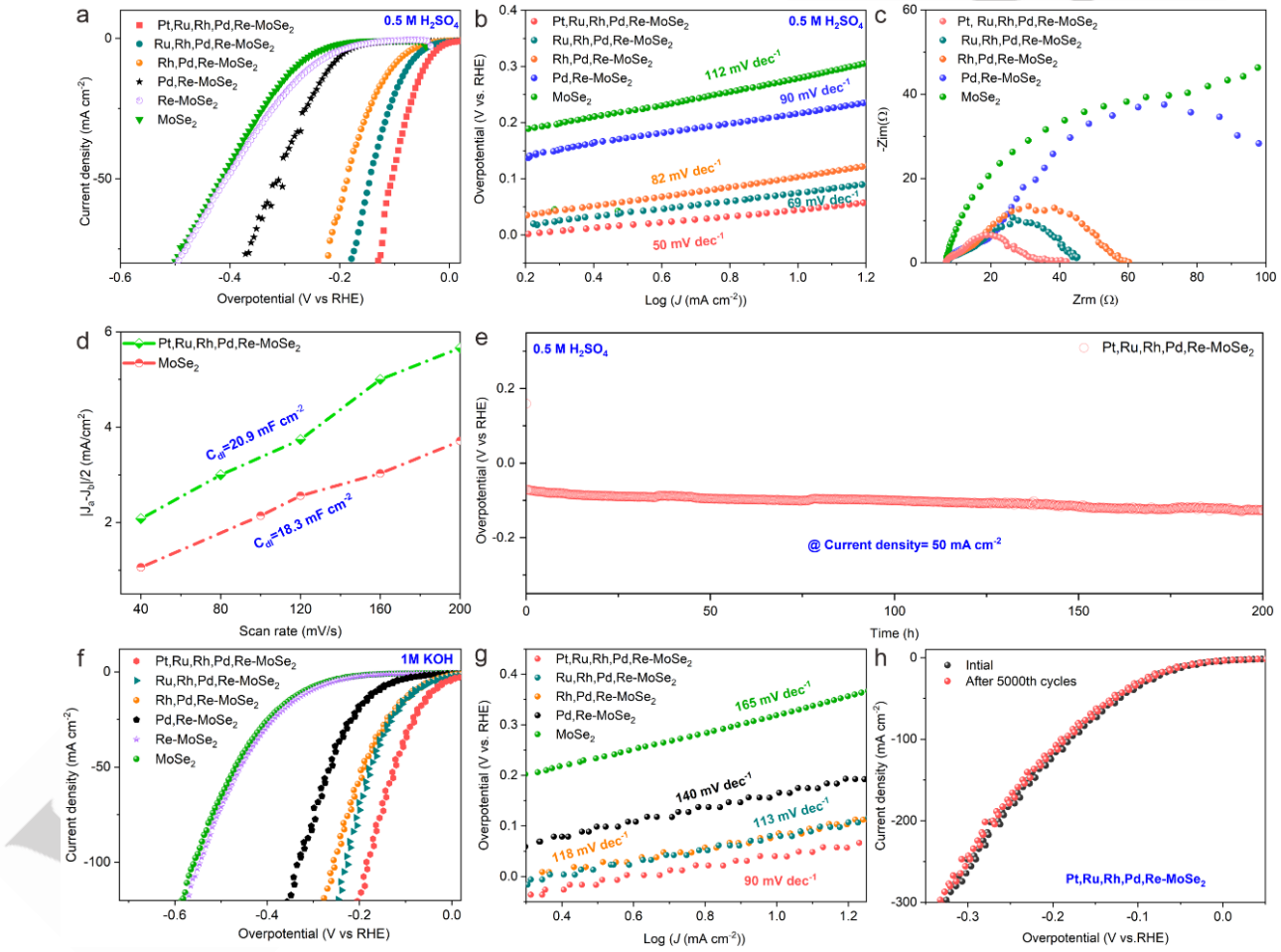

Figure 4. **a** HER polarization curves in acidic media. **b** Tafel slopes. **c** Nyquist plots. **d** The determination of C_{dl} by plotting the current density variation against the scan rates. **e** Long-term HER chronoamperometry test in 0.5 M H_2SO_4. **f** HER polarization curves in 1M KOH. **g** Corresponding Tafel slopes. **h** HER polarization curves of Pt,Ru,Rh,Pd,Re-$MoSe_2$ before and after 5000 cycles.

Encouraged by the successful preparation of a series of monometallic SAs, multimetallic SAs and high entropy SAs, we selected HER as the model reaction to evaluate the catalytic performance of TM-SAs/TMD catalysts. Compared to pristine TMD catalysts (Figure 4a and Figure S29), all TM-SAs/TMDs samples showed excellent HER activity in acidic media. The HER performance of the prepared catalysts follows the order of high SA/TMDs > quaternary SA/TMDs > ternary SA/TMDs > binary

SA/TMDs > SA/TMDs, indicating the HESAs exhibits the best HER activity. Excitingly, The overpotential of 10 mA cm^{-2} current density on Pt,Ru,Rh,Pd,Re-$MoSe_2$ (HESAs-01) is only 35 mV, which significantly exceeds most state-of-the-art SAs systems (Table S12) [10-11]. Furthermore, Pt,Ru,Rh,Pd,Re-$MoSe_2$ shows no observable performance decay after CO injection (Figure S30), indicating that the active in Pt,Ru,Rh,Pd,Re-$MoSe_2$ are distinct from that of metallic Pd, Pt, Rh and Ru[12]. Thus, the TM atom is not an active site, but acts by activating the inert TMD surface[13]. The corresponding Tafel diagram (Figure 4b) shows that TM-SAs doping reduces the Tafel slope from 102 to 50 mV dec^{-1}, suggesting that the HER process is faster and more reactive[14]. This transition is expected since TM-SAs doping leads to the formation of activated chalcogen atoms, which makes it easier to contact electrons and form H_{ads} at the interface. The superb activity of the Pt,Ru,Rh,Pd,Re-$MoSe_2$ catalyst is likewise evidenced by its specific activity, mass activity, turnover frequency (TOF) (Table S13), and charge transfer resistance (R_{ct}) derived from electrochemical impedance spectroscopy (EIS) (Figure 4c). Although the mass activity and TOF of Pt,Ru,Rh,Pd,Re-MoSe2 is still below that of Pt, it is better than those of the best-characterized TMDs-based materials. The introduction of TM-SAs may increase the structure disorder, thus improving the site density of final catalysts. Here, we further utilize cyclic voltammetry measurements to assess their relative electrochemically active surface areas by extracting double-layer capacitors (C_{dl})[15] (Figure 4d and Figure S31). The relative electrochemically active surface area of Pt,Ru,Rh,Pd,Re-$MoSe_2$ is similar to that of $MoSe_2$, revealing that the higher catalytic performance of Pt,Ru,Rh,Pd,Re-$MoSe_2$ is not due to the increase of accessible active sites[16]. In addition, Pt,Ru,Rh,Pd,Re-$MoSe_2$ is also stable long-life catalyst. The chronoamperometry (CP) test results (Figure 4e) showed that the Pt,Ru,Rh,Pd,Re-$MoSe_2$ exhibits an excellent catalytic durability over 200 h, and the observed potential increased by only 13 mV[7b, 11b]. The recycled Pt,Ru,Rh,Pd,Re-$MoSe_2$ that underwent the CP test bore no signs of aggregated TM atoms or TM-containing crystalline phases, showing the high stability of the HESAs attached to the TMDs (Figure S32).

It is clear that HER is more challenging in alkaline media than in acidic solution, owing to the sluggish water adsorption and dissociation dynamics[9, 13]. Figure 4f shows the HER polarization curves of $MoSe_2$, Re-$MoSe_2$, Pd,Re-$MoSe_2$, Rh,Pd,Re-$MoSe_2$, Ru,Rh,Pd,Re-$MoSe_2$, Pt,Ru,Rh,Pd,Re-$MoSe_2$ (HESAs-01) and Pt/C in 1 M KOH, in which the benchmark Pt (Figure S33) are used as control samples. First, the original $MoSe_2$ shows an overpotential of 10 mA cm^{-2} at 320 mV, consistent with the values reported in literature. Second, all TM-SAs/TMD catalytic systems showed much higher activity than pristine $MoSe_2$ catalyst. Specifically, HESAs-01 electrode (η = 32 mV@ 10 mA cm^{-2}, 120 mV@ 50 mA cm^{-2}) exhibits a breakthrough in the catalytic performance, which is significantly higher than that of the Pt (η= 75 mV @ 10 mA cm^{-2}, 218 mV @ 50 mA cm^{-2}). To our knowledge, this value is the highest activity ever reported for TMDs and SAs catalytic materials in an alkaline solution (Table S11)[7b, 17]. The corresponding Tafel plots (Figure 4g) show that TM-SAs doping reduces the Tafel slope from 165 to 90 mV dec^{-1}, indicating the overcome of water dissociation barrier. The Pt,Ru,Rh,Pd,Re-$MoSe_2$ catalyst also exhibits more than one magnitude increase in intrinsic activity (Table S14), evidenced by its superior specific activity, mass activity and TOF in alkaline media. Similarly, the Pt,Ru,Rh,Pd,Re-$MoSe_2$ electrode also exhibits good HER catalytic stability in alkaline media. As shown in Figure 4h, Pt,Ru,Rh,Pd,Re-MoSe2 exhibited good stability and no obvious overpotential increase during 5000 cycles. Moreover, the CP test results (Figure S34) also manifest that the Pt,Ru,Rh,Pd,Re-$MoSe_2$ shows a good long-term operational stability beyond 100 h with an observed potential increase of only 10 mV.

Until now, we have shown that high-entropy SAs greatly promote the HER performance of TMDs. In what follows, we try to decipher the modulation essence of the high entropy SAs dopants in HESAs-TMDs systems for HER catalysis at the atomic level. Our electrochemical data have demonstrated that the TM single atoms themselves do not contribute to HER activity[9-10]. Furthermore, we also calculated the H adsorption free energy (ΔG_H) on all high-entropy single atom sites, and found that these metal sites themselves (Pd, Rh, Ru, Rh) were calculated to be inactive as H does not form a very stable adsorption structure on these metal atop sites (Figure S35), which suggests that these TMs sites themselves are not active sites. By contrast, the ΔGH of the S atop sites adjacent to TM atoms (TM atoms: Pd, Rh, Ru, Rh) exhibit almost thermoneutral values among 0.15-0.18 eV (Figure 5a-d and Figure S36), indicating more favorable HER catalytic behavior than that of pristine $MoSe_2$ basal-plane. Thus, we think that the atomic-scale tailoring should regulate the adsorption state of hydrogen atoms on the TMDs surface of HESAs/TMDs systems because the introduction of high-entropy SAs may induce the charge redistribution and tune the electronic state of TMDs. First, ultraviolet photoelectron spectroscopy (UPS) (Figure 5e-h) was performed to study the electronic structure of HESAs-TMDs systems[16a]. For pristine TMDs, since the Fermi surface is isolated, and the absence of active electronic state leads to inertness in the 2H-TMDs plane (Figure 5i) [15, 18]. In contrast, p-d orbital hybridization between TM atoms and

10.1002/ange.202405017

coordinating atoms, such as S and Se, activates Mo-TM bonds[16b, 19], resulting in a narrower d-band around 0–6 eV compared to compared to the original TMDs. The positions of d-band center for Pt,Ru,Rh,Pd,Re-$MoSe_2$ (HESAs-01) and Pd,Ru,Rh,Pt,Re-MoS_2 (HESAs-02) were 4.57 eV and 4.61 eV, lower than those of $MoSe_2$ (5.56 eV) and MoS_2 (4.93 eV). The peak shift observed in the X-ray photoelectron spectra (Figure 5j and Figure S37) further confirms dopants induced Fermi level movement[20]. These results show that the active electron states of the TM and S atoms on the Fermi surface induce the charge redistribution of the S atom and adjust the electronic state of the S atom. In particular, the photoluminescence (PL) spectrum (Figure 5k) shows that HESAs induces the formation of metal-like electron band structures on TMDs. The macroscopic observations revealed that the electronic conductivity (Figure S38) of Pt,Ru,Rh,Pd,Re-$MoSe_2$ was more than one order of magnitude higher than that of $MoSe_2$, further demonstrating the effects of the high-entropy SAs dopants on the electronic properties.

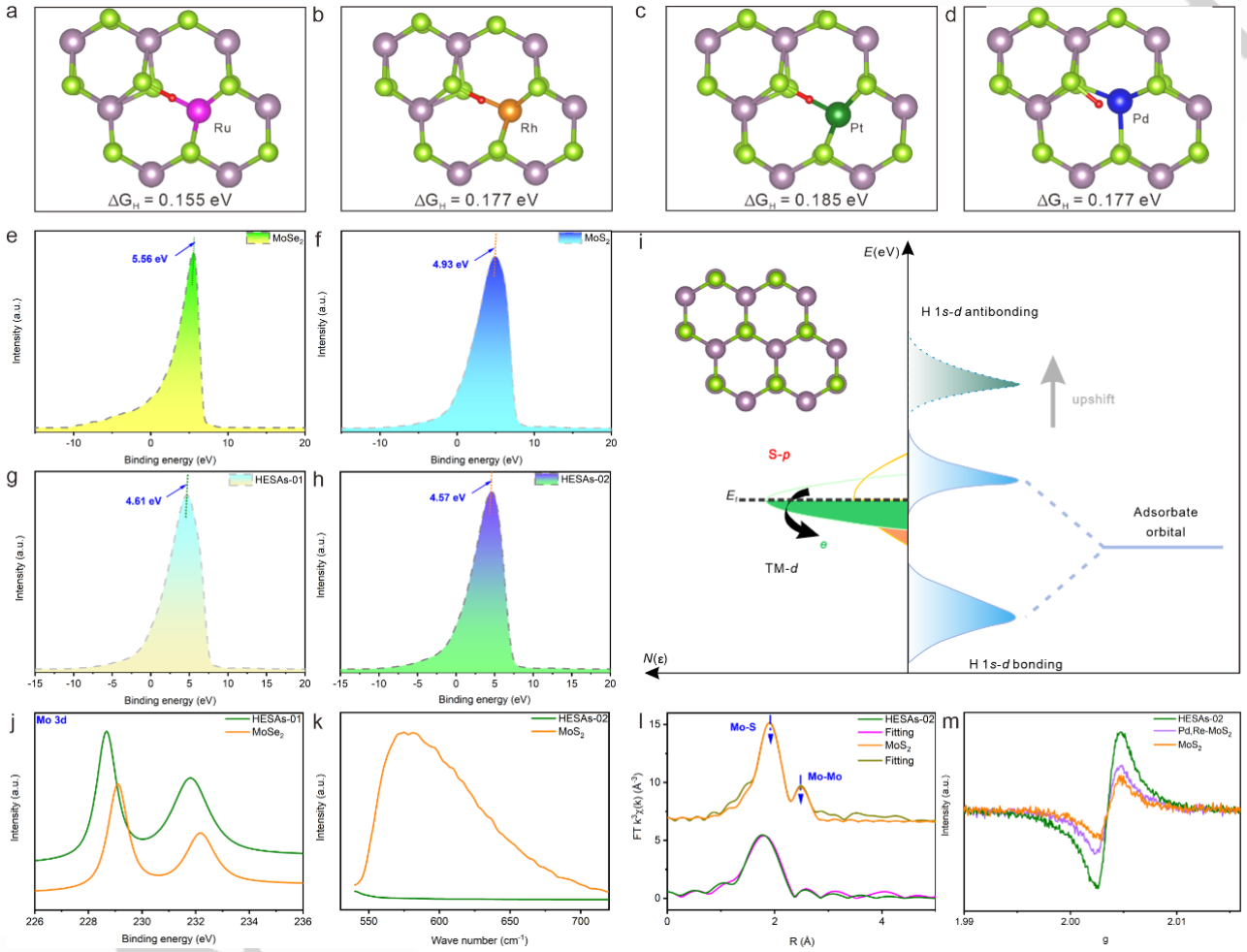

Figure 5. **a** Adsorption positions for single H atom absorbing at Ru site of $MoSe_2$. **b** Adsorption positions for single H atom absorbing at Rh site of $MoSe_2$. **c** Adsorption positions for single H atom absorbing at Pt site of $MoSe_2$. **d** Adsorption positions for single H atom absorbing at Pd site of $MoSe_2$. **e** Ultraviolet photoelectron spectroscopy (UPS) spectrum of $MoSe_2$. **f** UPS spectrum of MoS_2. **g** UPS spectrum of Pt,Ru,Rh,Pd,Re-$MoSe_2$. **h** UPS spectrum of Pt,Ru,Rh,Pd,Re-MoS_2. **i** Schematic DOS diagrams illustrating the high entropy effect on the d-band position of SAs-TMDs systems. **j** X-ray photoelectron spectroscopy (XPS) spectra of Mo 3d orbits of $MoSe_2$ and Pt,Ru,Rh,Pd,Re-$MoSe_2$. **k** Photoluminescence spectra of MoS_2 and Pt,Ru,Rh,Pd,Re-MoS_2. **l** Fourier transform of the k^3-weighted Mo K-edge of the EXAFS spectra of MoS_2 and Pt,Ru,Rh,Pd,Re-MoS_2. **m** Electron paramagnetic resonance (EPR) spectra of MoS_2 and Pt,Ru,Rh,Pd,Re-MoS_2.

Apart from tuning the electronic structure of TMDs, HESAs may also cause the creation of abundant SVs. It can be seen from the Mo K-edge EXAFS spectra in Figure 5i, two peaks at ~1.90 Å and ~2.92 Å are assigned to Mo–S and Mo–Mo scattering characteristics in TMDs. For example, the EXAFS spectrum of HESAs-02 shows a much weaker Mo-S peak intensity compared to MoS_2, due to the resulting SVs and interfacial effects between high-entropy SA species and MoS_2[17a, 21]. The Mo-Mo peak intensity of HESAs-02 is reduced compared to MoS_2, indicating a structural disturbance, which may be due to atomic rearrangement after TM atom substitution doping[18b, 22]. The same phenomenon occurs in other 2D materials ($MoSe_2$, $MoTe_2$) as

10.1002/ange.202405017

supports for SAs[23]. Electron paramagnetic resonance (EPR) spectroscopy (Figure 5m) was also carried out to probe the presence of unpaired electrons on coordinatively unsaturated sulfur defects[24]. The original MoS_2 material shows a relative low intensity at 2.56 × 10^4 a.u. mg^{-1} sites, which corresponds to the edge structures and crystallite interfaces. Notably, the TM-SAs/TMDs system demonstrated higher signal strength than MoS_2, confirming the formation of a large number of chalcogen defects, consistent with EXAFS results.

To demonstrate the practical application potential of the Pt,Ru,Rh,Pd,Re-$MoSe_2$ catalyst in water electrolysis, we further constructed an operational proton exchange membrane water electrolysis (PEMWE) system based on a membrane electrode assembly (MEA), employing Pt,Ru,Rh,Pd,Re-$MoSe_2$ and commercial Pt-C catalysts as the cathode catalyst and commercial IrO_2 as the anode. The steady-state polarization curves for the Pt,Ru,Rh,Pd,Re-$MoSe_2$-based PEMWE setups operated at 80 °C are shown in Figure 6a-c. Specifically, cell voltages of only 1.82 V and 1.98 V are needed to reach current densities of 1 and 1.5 A cm^{-2}, respectively. At low current density (0~0.8 A cm^{-2}), the PEMWE performance of Pt, Ru, Rh, Pd and Re-$MoSe_2$ catalysts is even higher than that of commercial Pt-C. To further validate the long-term operational stability of Pt,Ru,Rh,Pd,Re-$MoSe_2$ under real PEMWE conditions, we conducted an extended constant current electrolysis at a high current density of 1A cm^{-2} using a Pt,Ru,Rh,Pd,Re-$MoSe_2$ based MEA at 80 °C. As shown in Figure 6d, a negligible voltage decay of 10 mV was observed over the course of nearly 400 hours of water electrolysis. Thus, the excellent activity and stability of Pt,Ru,Rh,Pd,Re-$MoSe_2$ toward practical PEMWE applications is unambiguously verified.

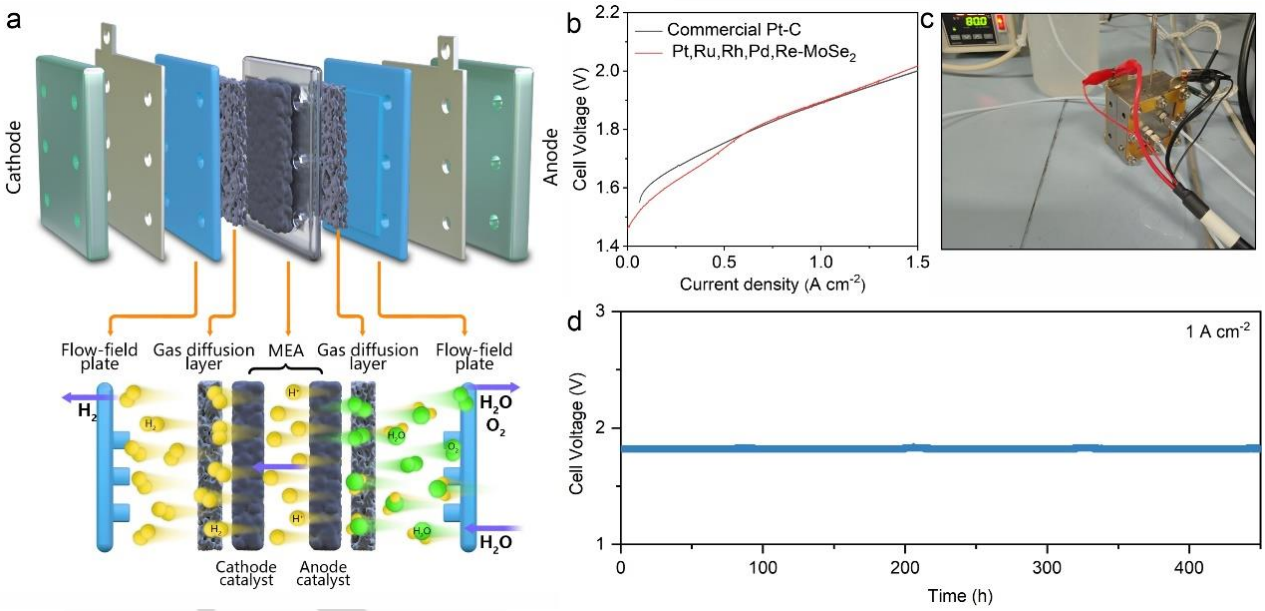

Figure 6. **a** Schematic diagram of the PEMWE electrolyzer. **b** Polarization curves of the PEMWE using the Pt,Ru,Rh,Pd,Re-$MoSe_2$ and commercial Pt-C catalyst as the cathode catalyst and commercial IrO_2 as the anode. **c** the photographs of the PEMWE device. **d** Chronopotentiometry curve of the PEMWE using Pt,Ru,Rh,Pd,Re-$MoSe_2$ operated at 1A cm^{-2}.

Conclusion

In summary, a spontaneous interfacial redox technique of creating and refilling of cation defects on TMDs (MoS_2, $MoSe_2$, etal) was developed to fabricate high loading of TM SAs on TMD supports. The approach appears to be versatile and can be used to prepare a library of reducible TMs (Pt, Pd, Ru, Ir, Rh and so on) SAs on TMDs. The driving power of Mo redox process and the strong metal−support interactions pushed the metal loading in single-atom catalysts to the limit, allowing a loading of SA-TMs up to 49 wt %. More specially, concentration-complex multimetallic SAs and high entropy SAs materials are also successfully synthesized through this a substrate-mediated SAs formation strategy. We further selected HER as a model reaction to evaluate the electrocatalytic activity of these polymetallic SAs and high-entropy SAs on $MoSe_2$, and found that this HESAs-TMDs system showed significant performance in the hydrogen evolution reaction compared to state-of-the-art TM-SAs and pristine TMDs systems. Thus, this study may open up exponentially more complex polymetallic phase spaces for SAs supported on TMD carriers and stimulate new areas of research for the discovery and optimization of SA-TMD catalytic systems, where the synergetic

co-catalysis of SA and TMD can be used to control SA-TMD activity and stability.

Acknowledgements

This work was financially supported by the National Natural Science Foundation of China (22109100), Guangdong Basic and Applied Basic Research Foundation (2024A1515012075, 2024A1515010028), Research Team Cultivation Program of ShenZhen University (2023QNT007). Thanks to Chuan Shi and Wei Zhang for their technical guidance in samples characterization, and Instrumental Analysis Center of Shenzhen University. The authors also appreciate the help of the beamline scientist of HXMA (Dr. Weifeng Chen), VESPERS (Dr. Renfei Feng), PGM (Dr. Lucia Zuin), BXDS, and SXRMB (Dr. Mohsen Shakouri, Dr. Qundeng Xiao, and Dr. Yongfeng Hu) beambine at Canadian Light Source. The authors wish to acknowledge the assistance on HRTEM observation received from the Electron Microscope Center of the Shenzhen University.

Conflict of interest

There are no conflicts to declare.

Keywords: Two-dimensional transition-metal dichalcogenides, high-entropy single-atom catalysts, reducible metals, spontaneous interfacial redox reaction, hydrogen evolution reaction

[1] aH. Bai, D. Chen, Q. Ma, R. Qin, H. Xu, Y. Zhao, J. Chen, S. Mu, *Electrochemical Energy Reviews* **2022**, *5*; bF. Si, S. Liu, Y. Liang, X.-Z. Fu, J. Zhang, J.-L. Luo, *Electrochemical Energy Reviews* **2022**, *5*; cX. Wang, Q. Hu, G. Li, H. Yang, C. He, *Electrochemical Energy Reviews* **2022**, *5*.

[2] aH. Yin, P. Yuan, B.-A. Lu, H. Xia, K. Guo, G. Yang, G. Qu, D. Xue, Y. Hu, J. Cheng, S. Mu, J.-N. Zhang, *ACS Catalysis* **2021**, *11*, 12754-12762; bX. Xie, C. He, B. Li, Y. He, D. A. Cullen, E. C. Wegener, A. J. Kropf, U. Martinez, Y. Cheng, M. H. Engelhard, M. E. Bowden, M. Song, T. Lemmon, X. S. Li, Z. Nie, J. Liu, D. J. Myers, P. Zelenay, G. Wang, G. Wu, V. Ramani, Y. Shao, *Nature Catalysis* **2020**, *3*, 1044-1054; cA. Mehmood, M. Gong, F. Jaouen, A. Roy, A. Zitolo, A. Khan, M.-T. Sougrati, M. Primbs, A. M. Bonastre, D. Fongalland, G. Drazic, P. Strasser, A. Kucernak, *Nature Catalysis* **2022**, *5*, 311-323.

[3] aH. Fei, J. Dong, Y. Feng, C. S. Allen, C. Wan, B. Volosskiy, M. Li, Z. Zhao, Y. Wang, H. Sun, P. An, W. Chen, Z. Guo, C. Lee, D. Chen, I. Shakir, M. Liu, T. Hu, Y. Li, A. I. Kirkland, X. Duan, Y. Huang, *Nature Catalysis* **2018**, *1*, 63-72; bH. Xie, X. Xie, G. Hu, V. Prabhakaran, S. Saha, L. Gonzalez-Lopez, A. H. Phakatkar, M. Hong, M. Wu, R. Shahbazian-Yassar, V. Ramani, M. I. Al-Sheikhly, D.-e. Jiang, Y. Shao, L. Hu, *Nature Energy* **2022**, *7*, 281-289.

[4] aJ.-C. Liu, H. Xiao, J. Li, *Journal of the American Chemical Society* **2020**, *142*, 3375-3383; bY. Nakaya, E. Hayashida, H. Asakura, S. Takakusagi, S. Yasumura, K. I. Shimizu, S. Furukawa, *J Am Chem Soc* **2022**, *144*, 15944-15953; cJ. Zhang, X. Tian, M. Liu, H. Guo, J. Zhou, Q. Fang, Z. Liu, Q. Wu, J. Lou, *J Am Chem Soc* **2019**, *141*, 19269-19275.

[5] aW. Wu, C. Niu, C. Wei, Y. Jia, C. Li, Q. Xu, *Angew Chem Int Ed Engl* **2019**, *58*, 2029-2033; bL. Zhang, R. Si, H. Liu, N. Chen, Q. Wang, K. Adair, Z. Wang, J. Chen, Z. Song, J. Li, M. N. Banis, R. Li, T. K. Sham, M. Gu, L. M. Liu, G. A. Botton, X. Sun, *Nat Commun* **2019**, *10*, 4936.

[6] aP. Rao, Y. Deng, W. Fan, J. Luo, P. Deng, J. Li, Y. Shen, X. Tian, *Nat Commun* **2022**, *13*, 5071; bF. Xiao, Q. Wang, G.-L. Xu, X. Qin, I. Hwang, C.-J. Sun, M. Liu, W. Hua, H.-w. Wu, S. Zhu, J.-C. Li, J.-G. Wang, Y. Zhu, D. Wu, Z. Wei, M. Gu, K. Amine, M. Shao, *Nature Catalysis* **2022**, *5*, 503-512.

[7] aY. Guo, R. Zhang, S. Zhang, H. Hong, Y. Zhao, Z. Huang, C. Han, H. Li, C. Zhi, *Energy & Environmental Science* **2022**, *15*, 4167-4174; bA. R. Puente Santiago, T. He, O. Eraso, M. A. Ahsan, A. N. Nair, V. S. N. Chava, T. Zheng, S. Pilla, O. Fernandez-Delgado, A. Du, S. T. Sreenivasan, L. Echegoyen, *J Am Chem Soc* **2020**, *142*, 17923-17927; cT. Zheng, C. Liu, C. Guo, M. Zhang, X. Li, Q. Jiang, W. Xue, H. Li, A. Li, C. W. Pao, J. Xiao, C. Xia, J. Zeng, *Nat Nanotechnol* **2021**, *16*, 1386-1393.

[8] Y. Zhou, J. Zhang, E. Song, J. Lin, J. Zhou, K. Suenaga, W. Zhou, Z. Liu, J. Liu, J. Lou, H. J. Fan, *Nat Commun* **2020**, *11*, 2253.

[9] Z. Luo, H. Zhang, Y. Yang, X. Wang, Y. Li, Z. Jin, Z. Jiang, C. Liu, W. Xing, J. Ge, *Nat Commun* **2020**, *11*, 1116.

[10] Z. Y. Luo, J. J. Li, Y. L. Li, D. J. Wu, L. Zhang, X. Z. Ren, C. X. He, Q. L. Zhang, M. Gu, X. L. Sun, *Advanced Energy Materials* **2022**, *12*.

[11] aZ. Luo, Y. Ouyang, H. Zhang, M. Xiao, J. Ge, Z. Jiang, J. Wang, D. Tang, X. Cao, C. Liu, W. Xing, *Nat Commun* **2018**, *9*, 2120; bB. Wang, X. Zhu, X. Pei, W. Liu, Y. Leng, X. Yu, C. Wang, L. Hu, Q. Su, C. Wu, Y. Yao, Z. Lin, Z. Zou, *Journal of the American Chemical Society* **2023**, *145*, 13788-13795.

[12] Y. Xia, S. Guo, L. Yang, S. He, L. Zhou, M. Wang, J. Gao, M. Hou, J. Wang, S. Komarneni, *Adv Mater* **2023**, e2303523.

[13] K. Jiang, M. Luo, Z. Liu, M. Peng, D. Chen, Y. R. Lu, T. S. Chan, F. M. F. de Groot, Y. Tan, *Nat Commun* **2021**, *12*, 1687.

[14] Z. Wang, B. Xiao, Z. Lin, Y. Xu, Y. Lin, F. Meng, Q. Zhang, L. Gu, B. Fang, S. Guo, W. Zhong, *Angew Chem Int Ed Engl* **2021**, *60*, 23388-23393.

[15] X. Wang, Y. Zhang, H. Si, Q. Zhang, J. Wu, L. Gao, X. Wei, Y. Sun, Q. Liao, Z. Zhang, K. Ammarah, L. Gu, Z. Kang, Y. Zhang, *J Am Chem Soc* **2020**, *142*, 4298-4308.

[16] aY. Shi, W. M. Huang, J. Li, Y. Zhou, Z. Q. Li, Y. C. Yin, X. H. Xia, *Nat Commun* **2020**, *11*, 4558; bJ. Peto, T. Ollar, P. Vancso, Z. I. Popov, G. Z. Magda, G. Dobrik, C. Y. Hwang, P. B. Sorokin, L. Tapaszto, *Nature Chemistry* **2018**, *10*, 1246-1251.

[17] aY. Li, Q. Gu, B. Johannessen, Z. Zheng, C. Li, Y. Luo, Z. Zhang, Q. Zhang, H. Fan, W. Luo, B. Liu, S. Dou, H. Liu, *Nano Energy* **2021**, *84*; bD. Hu, T. Zhao, X. Ping, H. Zheng, L. Xing, X. Liu, J. Zheng, L. Sun, L. Gu, C. Tao, D.

10.1002/ange.202405017

Wang, L. Jiao, *Angew Chem Int Ed Engl* **2019**, *58*, 6977-6981; cJ. Qin, C. Xi, R. Zhang, T. Liu, P. Zou, D. Wu, Q. Guo, J. Mao, H. Xin, J. Yang, *ACS Catalysis* **2021**, *11*, 4486-4497; dE. E. Benson, H. Zhang, S. A. Schuman, S. U. Nanayakkara, N. D. Bronstein, S. Ferrere, J. L. Blackburn, E. M. Miller, *J Am Chem Soc* **2018**, *140*, 441-450.

[18] aS. Karunakaran, S. Pandit, B. Basu, M. De, *J Am Chem Soc* **2018**, *140*, 12634-12644; bK. Qi, X. Cui, L. Gu, S. Yu, X. Fan, M. Luo, S. Xu, N. Li, L. Zheng, Q. Zhang, J. Ma, Y. Gong, F. Lv, K. Wang, H. Huang, W. Zhang, S. Guo, W. Zheng, P. Liu, *Nat Commun* **2019**, *10*, 5231.

[19] aN. Salazar, S. Rangarajan, J. Rodriguez-Fernandez, M. Mavrikakis, J. V. Lauritsen, *Nat Commun* **2020**, *11*, 4369; bY. Fang, J. Pan, J. He, R. Luo, D. Wang, X. Che, K. Bu, W. Zhao, P. Liu, G. Mu, H. Zhang, T. Lin, F. Huang, *Angew Chem Int Ed Engl* **2018**, *57*, 1232-1235.

[20] aA. P. Gaur, S. Sahoo, M. Ahmadi, S. P. Dash, M. J. Guinel, R. S. Katiyar, *Nano Lett* **2014**, *14*, 4314-4321; bK. C. Santosh, R. C. Longo, R. M. Wallace, K. Cho, *J Appl Phys* **2015**, *117*.

[21] J. Deng, H. Li, J. Xiao, Y. Tu, D. Deng, H. Yang, H. Tian, J. Li, P. Ren, X. Bao, *Energy & Environmental Science* **2015**, *8*, 1594-1601.

[22] X. Guo, E. Song, W. Zhao, S. Xu, W. Zhao, Y. Lei, Y. Fang, J. Liu, F. Huang, *Nat Commun* **2022**, *13*, 5954.

[23] aY. Liu, X. Hu, J. Li, G. Zhong, J. Yuan, H. Zhan, Y. Tang, Z. Wen, *Nat Commun* **2022**, *13*, 663; bJ. Chen, X. Zhao, S. J. Tan, H. Xu, B. Wu, B. Liu, D. Fu, W. Fu, D. Geng, Y. Liu, W. Liu, W. Tang, L. Li, W. Zhou, T. C. Sum, K. P. Loh, *J Am Chem Soc* **2017**, *139*, 1073-1076.

[24] aJ. Xu, G. Shao, X. Tang, F. Lv, H. Xiang, C. Jing, S. Liu, S. Dai, Y. Li, J. Luo, Z. Zhou, *Nat Commun* **2022**, *13*, 2193; bY. Lou, Y. Zheng, X. Li, N. Ta, J. Xu, Y. Nie, K. Cho, J. Liu, *J Am Chem Soc* **2019**, *141*, 19289-19295; cJ. Hu, L. Yu, J. Deng, Y. Wang, K. Cheng, C. Ma, Q. Zhang, W. Wen, S. Yu, Y. Pan, J. Yang, H. Ma, F. Qi, Y. Wang, Y. Zheng, M. Chen, R. Huang, S. Zhang, Z. Zhao, J. Mao, X. Meng, Q. Ji, G. Hou, X. Han, X. Bao, Y. Wang, D. Deng, *Nature Catalysis* **2021**, *4*, 242-250.